Integrated graphene quantum dot decorated functionalized nanosheet biosensor for mycotoxin detection

Hema Bhardwaj [1,2] · Christophe A. Marquette [3] · Priyanka Dutta [1,2] · Rajesh [1] · Gajjala Sumana [1,2]

Abstract

Decoration of graphene quantum dots (GQDs) on molybdenum disulfide (MoS_2) nanosheets serves as an active electrode material which enhances the electrochemical performance of the analyte detection system. Herein, ionic surfactant cetyltrimethylammonium bromide (CTAB)-exfoliated MoS_2 nanosheets decorated with GQD material are used to construct an electrochemical biosensor for aflatoxin B1 (AFB1) detection. An antibody of AFB1 (aAFB1) was immobilized on the electrophoretically deposited MoS_2@GQDs film on the indium tin oxide (ITO)-coated glass surface using a crosslinker for the fabrication of the biosensor. The immunosensing study investigated by the electrochemical method revealed a signal response in the range of 0.1 to 3.0 ng/mL AFB1 concentration with a detection limit of 0.09 ng/mL. Also, electrochemical parameters such as diffusion coefficient and heterogeneous electron transfer (HET) were calculated and found to be 1.67×10^{-5} cm^2/s and 2×10^{-5} cm/s, respectively. The effective conjugation of MoS_2@GQDs that provides abundant exposed edge sites, large surface area, improved electrical conductivity, and electrocatalytic activity has led to an excellent biosensing performance with enhanced electrochemical parameters. Validation of the fabricated immunosensor was performed in a spiked maize sample, and a good percentage of recoveries within an acceptable range were obtained (80.2 to 98.3%).

Keywords Molybdenum disulfide · Graphene quantum dots · Electrochemical impedance spectroscopy · Immunosensor · Aflatoxin B1

Introduction

Worldwide contamination in food products by mycotoxins is a critical concern leading to causes of industrial and agricultural losses of billions of dollars, and their consumption shows a significant impact on human health and animal welfare [1]. Among the various mycotoxins, AFB1 is one of the potent toxins produced by multiple strains of the fungus, i.e., *Aspergillus flavus*, and *Aspergillus parasiticu*s under specific temperature (24–36 °C), and humid conditions (> 7%). AFB1 occurring in the food includes grains, maize, groundnuts, and peanuts [2, 3]. AFB1 responsible for severe consequences from acute hepatic toxicity to chronic diseases includes liver cancer and edema, and also caused death of a person. It is classified as a group-I human carcinogen by the International Agency for Research on Cancer (IARC) [4]. Many conventional techniques available are high-performance liquid chromatography (HPLC), thin layer chromatography (TLC), and liquid chromatography (LC) combined with mass spectroscopy (MS). Still, these are time-consuming, well-equipped laboratory required, and need personnel trained for the analysis.

In recent years, enhanced biosensing performances obtained in terms of cost-effective transducer material, sensitivity, and selective response in a short duration of time due to the integration of nanomaterials into biosensor device. Earlier, we have published a research article on GQD-gold nanoparticle (AuNP) composite integrated surface matrix for AFB1

✉ Gajjala Sumana
sumanagajjala@gmail.com

1   CSIR-National Physical Laboratory, Dr. KS Krishnan Marg, New Delhi 110012, India

2   Academy of Scientific and Innovative Research (AcSIR), Ghaziabad 201002, India

3   3d.FAB, CNRS, INSA, CPE-Lyon, ICBMS, University Lyon1, 69100 Villeurbanne cedex, France

detection using cyclic voltammetry (CV) technique [5]. Though the sensor has shown high performance for the detection of food toxin, in the case of low concentration, the significant linear change in the voltammetry peak height has been obtained. As by increasing the AFB1 concentration, voltammetry waves are merged and migrated towards the higher potential side due to the electron transfer kinetics of the quasi-reversible process. But, in the current article, the electrochemical impedance spectroscopy technique has been used to investigate the bioanalytical sensing performance. Impedimetric sensor involves more advantages towards the biosensing characteristics which gives relevant information about electrokinetic parameters, i.e., double-layer capacitance (C_{dl}), quality of impedance spectrum response by Kramers-Kronig (K-K) test, analysis of computer-simulated fitting using different electronic circuit elements to obtain the best fit of spectra, and interfacial properties to understand the electrochemical process.

Among the various materials, two-dimensional (2D) nanosheets such as graphene oxide, reduced graphene oxide, MoS_2 nanosheets have extensively been utilized in many applications such as photovoltaic devices [6], lithium-ion batteries [7], hydrogen evolution [8], DNA detection [9], photodetectors [10], and biosensors [11], due to their unique optical, electrical, and catalytic properties [12]. Among these, MoS_2 nanosheets exhibit excellent electrochemical properties, including low R_{CT}, exclusive electrocatalytic property, conductivity, and large surface area. The presence of these superb chemical and electrical properties of MoS_2 nanosheets are well-suited for the electrical bio-system [13]. For example, Huang et al. developed a glucose biosensor using the nanohybrid system as a nickel nanoparticle that have 6 nm of average diameter and MoS_2 nanosheets. With excellent sensitivity, catalytic activity with low expense was achieved due to the impact of advanced hybrid nanomaterial biosensor [14]. Structurally, MoS_2 nanosheets have hexagonal crystallite lattice ordered in a manner of S-Mo-S through van der Waals interactions where each sheet is made up of three layers comprising a molybdenum atom between the two layers of the sulfur atom [15]. These sheets exhibit significant intrinsic band gap and considerable charge carrier mobility in a single layer or few layer in comparison with other materials that have an insignificant band gap, such as graphene. For the preparation of a single layer or few layers of MoS_2 nanosheets, several methods have been reported, such as liquid exfoliation, ball milling, chemical vapor deposition, and electrochemical lithium intercalation [16]. These methods required an extended processing time, and the use of toxic solvent has certain limitations. Therefore, in this context, a simple route of chemical exfoliation of solid MoS_2 to MoS_2 nanosheets in an aqueous solution of the ionic surfactant of CTAB has been adopted to form good quality of nanosheets with higher yield [17]. Both theoretical and experimental studies revealed MoS_2

nanosheet edge planes show an active contribution to improving electronic conductivity. In contrast, inert basal planes exhibit an insignificant active number of sites along with lower catalytic activity [18].

The decoration of MoS_2 nanosheets with nanomaterial leads to improving a significant number of active sites that increase the vertical charge transportation [19]. The tremendous interest existing in graphene shows potential applications in an electronic, fuel cell, transistors, biosensor, or bioimaging areas, but intrinsic properties such as electrical or optical can be improved by cutting the lateral dimensional size, i.e., from graphene oxide to GQDs [20]. GQDs exhibit excellent electrical and optical properties such as catalytic property, defect-free aromatic structure, functional groups, biocompatibility, conductivity, solubility, and large surface-to-volume ratio. The abundance of carboxylic groups enhanced antibody absorption on the electrode surface, increase mass transfer electroactive species, stabilization, and electrochemical response signal of the device. Therefore, decoration of GQDs on MoS_2 nanosheets by synergistic effect reduces the restacking tendency of nanosheets, overcomes charge incompatibility, and increases bioconjugation capability that helps to improve the bio-analyte system performance [21, 22]. MoS_2@GQDs also enhances electronic conductivity; provides a large active surface area, which helps to attain high permeability and adhesion, non-toxicity, high carrier mobility, and reduction of internal resistance; and improves charge transportation of electronic devices [23]. In this context, we have demonstrated a label-free electrochemical ultrasensitive strategy for AFB1 detection using MoS_2@GQDs as an electrode surface transducer material. The proposed as-prepared biosensing device shows sensitive, reliable, and selective detection of AFB1.

Experimental details

Chemicals

The antibody and antigen of AFB1 were procured from Sigma-Aldrich. MoS_2 powder (99.99%), CTAB, N-ethyl-N-(3-dimethylamino propyl) carbodiimide (EDC), N-hydroxysuccinimide (NHS), ammonia (NH_3), hydrogen peroxide (H_2O_2), potassium ferrocyanide [$K_4(Fe(CN)_6)$], potassium ferricyanide [$K_3(Fe(CN)_6)$], bovine serum albumin (BSA), and all other chemicals were purchased from Sigma-Aldrich, India, and used as such without further purification. Milli-Q purified water resistivity of 18.2 MΩ.cm was used for the preparation of buffer and all other required solutions. The stock of AFB1 completely dissolved in a moderately polar organic solvent as dimethyl sulfoxide, and aqueous dilutions

of AFB1 were prepared in 50 mM phosphate buffer saline (PBS, pH 7.4).

Synthesis of CTAB-exfoliated MoS₂ nanosheets

MoS_2 nanosheets were prepared using the earlier reported method [17]. In detail, 300 mg of MoS_2 powder was dispersed in 30 mL of CTAB solution and kept on ultrasonication for 8 h at 100 W. An aqueous dispersed solution of black solid MoS_2 powder was converted into MoS_2 nanosheets contained a single layer or few layer of sheets. Rapid compression, along with rarefaction sound waves, creates a vacuum cavity within the reaction medium and generates high pressure inside the reaction mixture that easily peels off the MoS_2 layers [17, 24]. Afterward, MoS_2 nanosheets were purified by centrifugation at 2795g for 30 min and washed with distilled water.

Synthesis of GQDs and MoS₂@GQD composite

GQDs were synthesized using our previously reported method [25] and prepared GQDs, and MoS_2 nanosheets were used for the preparation of composite MoS_2@GQDs. In brief, 20 mg of CTAB-functionalized MoS_2 nanosheets was poured in 10 mL of distilled water and kept on stirring for 20 min. After that, GQDs (0.5 mg/mL) were added to the above resultant solution and was further stirred for 3 h at about 40 °C, and the resulting suspension was centrifuged at 1006g for 10 min to obtain the desired product.

Instrumentation

The ultraviolet-visible absorbance study was carried out using a UV-visible spectrophotometer (Phoenix-2200DPCV) at room temperature. Fourier transform infrared (FT-IR) studies were performed using the Perkin-Elmer Spectrum BX II spectrophotometer with germanium waveguide by average 64 scans at resolution 4 cm^{-1}. The structural analysis was performed using a high-resolution transmission electron microscope (HR-TEM, Techaii-G2F30 STWIN). The crystalline structure and planes determined using the X-ray diffraction (XRD) technique under Cu Kα (λ = 0.154 nm) radiation Rigaku. Raman spectrum analysis of the MoS_2 nanosheets and composite of MoS_2@GQDs was performed using the Renishaw Raman spectrometer (micro Raman model in Via reflex) with a laser excitation wavelength of 514 nm. Morphological analysis of MoS_2@GQDs and immobilized aAFB1 on MoS_2@GQDs/ITO electrode were examined by a scanning electron microscope (SEM, JEOL JSM-35). Zeta-potential was determined by Malvern Zetasizer Nano ZS90 at a scattering angle 90°. All the electrochemical measurements such as CV (potential range + 0.75 to − 0.75 V, scan rate 50 mV/s) and electrochemical impedance spectroscopy (EIS, A. C mode: single sine, perturbing potential at

0.25 V in the frequency range of 0.1 to 10^4 Hz, 10 points per decade, 0 s time to wait, 0.01 V of amplitude (RMS) and 1-s integration time) have been carried out in a three-electrode cell. Cell comprises platinum as a counter electrode (2×1 cm^2), aAFB1/MoS₂@GQDs/ITO as a working electrode (2×1 cm^2), and Ag/AgCl as a reference electrode in phosphate buffer saline (50 mM, pH 7.4, 0.9% NaCl) containing 5 mM of $[Fe(CN)_6]^{3-}$ and $[Fe(CN)_6]^{4-}$. Before conducting the electrochemical experiments, a freshly same day prepared redox probe was used to carry out the electrochemical measurements under the ambient atmospheric temperature condition using a galvanostat/potentiostat Autolab (PGSTAT 302N system, Eco Chemie, the Netherlands).

Preparation of aAFB1/MoS₂@GQD immunosensor for AFB1 detection

ITO-coated glass electrodes were first cleaned by distilled water then rinsed with ethanol solution. Cleaned ITO slides were dipped in a solution mixture of H_2O_2:NH_3:H_2O (1:1:5 v/v) and heated at 80 °C for 30 min for surface oxidation, followed by drying at room temperature. An immense film of MoS_2@GQDs on the ITO slide was obtained using the electrophoretic deposition technique. A stock aqueous solution of 1 mg/mL of MoS_2@GQDs was prepared, and 1 mL of this suspension was poured into a two-electrode cell containing an aqueous dispersion of 10^{-4} mol of Mg $(NO_3)_2$.$6H_2O$. Ten volt for 1 min was applied to obtain the uniform deposition. After the successful deposition of MoS_2@GQDs, the resultant ITO slides were washed with distilled water and dried at room temperature. Furthermore, the surface functional groups of MoS_2@GQDs/ITO electrode were activated by EDC:NHS zero-length crosslinker [1:1 (v/v) of EDC (0.2 M) and NHS (0.05 M)]. Here, 10 μL of the crosslinker reaction mixture was poured on MoS_2@GQDs/ITO surface and kept in a humid chamber for 4 h at room temperature. Then an optimized concentration 80 μg/mL of aAFB1 was immobilized over the activated MoS_2@GQDs/ITO surface and kept 12 h at room temperature [26], followed by washing thoroughly with PBS to remove unbound aAFB1. Then surface modified electrodes were treated with 1% of BSA solution to block non-specific interactions sites. Strong chemically covalent antibody conjugation to functional groups of GQDs and MoS_2 nanosheet surface, provides a benign environment and enhance the stabilization parameter of the electrode. The fabricated aAFB1/MoS₂@GQDs/ITO electrodes were kept in the refrigerator (4 °C) when not in use.

Preparation of real samples

Fresh maize samples were purchased from the local market and analyzed before their expiration dates. First, samples were ground to powder in a household blender. One gram of maize

was spiked with 200 μL of antigen AFB1 concentrations of 0.1, 0.25, and 0.5 mg/mL solutions [27–29] and left at room temperature for 1 h. For standard AFB1 sample preparation, stock of AFB1 completely dissolved in a moderately polar organic solvent as dimethyl sulfoxide using the specified method [30] then dilutions were made in 50 mM PBS solution. After that, the extraction of spiked samples was prepared in 20 mL of 80/20 (v/v) of methanol/water and gently stirred for 2 h at room temperature. The use of water in the extraction procedure usually increases the extraction efficiency because water can break the interactions between toxins and other sample constituents and subsequently improve the penetration of the solvent into the material [31]. To dispose of excess solvent, centrifugation was performed at 2795g for 30 min. The supernatant was carefully collected, and dilutions were made using 1:5 (v/v) of PBS. Similarly, a non-spiked sample was prepared using the above procedure without the addition of analyte AFB1. Then, prepared samples were analyzed using fabricated immunosensor.

Results and discussion

Structural and morphological characterization

Figure 1 illustrates the diagrammatic representation of the synthesis of MoS$_2$@GQD material using functionalized CTAB-MoS$_2$ nanosheets and GQDs, followed by deposition on the ITO glass electrode surface and fabrication of electrochemical immunosensor for AFB1 detection using electrochemical detection technique.
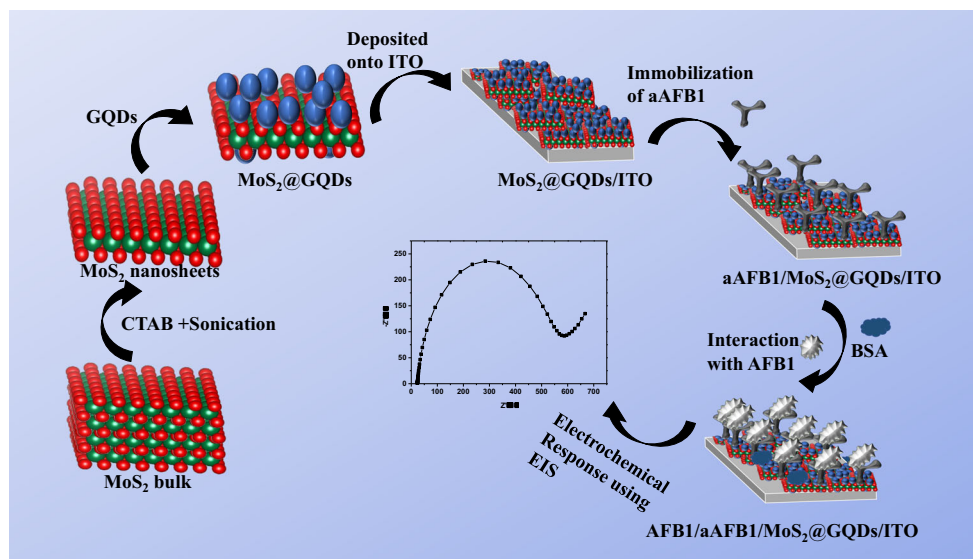
Figure 2 a displays the UV-visible spectrum of MoS$_2$ nanosheets (curve i) and MoS$_2$@GQD composite (curve ii). The optical spectrum of MoS$_2$ nanosheets shown in curve i, the peak at 468 nm assigned to transition from valence to conduction band whereas other distinct broad humps appearing at 625 nm and 663 nm attributed to K point of Brillouin zone confirm the formation of MoS$_2$ nanosheets [32]. These two low energy absorption peaks are known to correspond to the excitonic transition occurring between the splitter valence bands and conductance bands of MoS$_2$ nanosheets [33]. MoS$_2$@GQD composite absorption curve is displayed in Fig. 2 a curve ii. Apart from the appearance of the above mentioned MoS$_2$ peaks (curve i), here, additional absorption peak appeared at 328 nm, which corresponds to n-π^* transition of GQDs indicating the presence of C–O and aromatic C=C bonds. However, a slight shift in the absorbance appearing at 476 nm, 646 nm, and 680 nm (curve ii) is due to the absorption band of MoS$_2$ nanosheets. The results indicate the conjugation and formation of MoS$_2$ and GQD composite.

The crystallinity and diffraction studies of MoS$_2$ nanosheets and MoS$_2$@GQD composite were investigated by XRD technique (see Electronic Supplementary Material (ESM) Fig. S1). The XRD spectra of MoS$_2$ nanosheets show in the inset image a sharply intense peak appearing at 13.96° corresponding to 002 planes of pure MoS$_2$ nanosheets. And, d-spacing found to be 0.64 nm belongs to the hexagonal MoS$_2$ crystalline structure indexed (JCPDS card no. 37-1492). Moreover, distinct peaks appearing at 33.27°, 39.47°, 49.07°, 58.63°, and 69.80° correspond to diffraction planes of (100), (103), (006), (105), and (110), respectively, indicating well-stacked layered structure formation and the results are in agreement with the reported XRD data of MoS$_2$

Fig. 1 Schematic illustrations of electrochemical biosensor for aflatoxin B1 detection using MoS$_2$@GQD composite

Fig. 2 **a** UV-vis absorbance spectrum of (i) MoS_2 nanosheets and (ii) MoS_2@GQD composite in aqueous medium. **b** FT-IR of (i) MoS_2/ITO, (ii) MoS_2@GQDs/ITO composite, and (iii) biomolecule immobilized electrode aAFB1/MoS_2@GQDs/ITO. **c** Raman spectrum of MoS_2@GQDs (inset image: Raman spectrum of MoS_2)
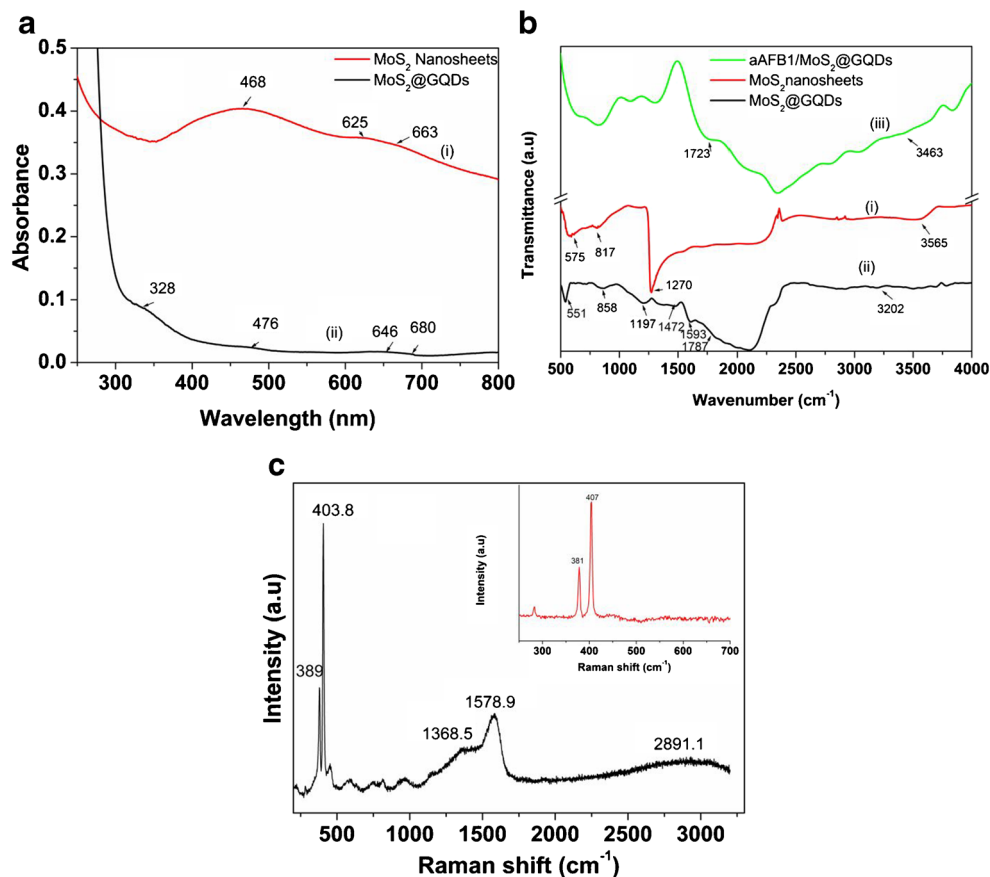
nanosheets [34]. Furthermore, the XRD pattern of MoS_2@GQD composite shows the peak at 23.3° corresponding to (002) planes of GQDs. Also, several diffraction peaks appearing at 12.7°, 30.14°, 33.3°, and 60.48° correspond to MoS_2 nanosheets confirming the formation of MoS_2@GQD composite. However, in the spectrum of MoS_2@GQD composite, some additional diffraction peaks also appeared at 35.43° and 50.73° corresponding to (400) and (440) reflection planes, respectively, due to the ITO-coated glass substrate [34].

The presence of functional groups, bonding, and conjugation of the bio-nano film is confirmed by the FT-IR technique. Figure 2 b demonstrates the FT-IR spectrum of MoS_2 nanosheets (curve i), MoS_2@GQD composite (curve ii), and biomolecule immobilized aAFB1/MoS_2@GQDs electrode (curve iii). As seen from Fig. 2 b (i), a distinct peak appeared at 575 cm^{-1} assigned to –C–Br CTAB stretching bond formation and other peaks at 817 and 1270 cm^{-1} may be responsible for –C–H and –C–N bonds in CTAB, respectively [35]. Also, an infrared peak found at 3565 cm^{-1} may be assigned to the linkage of Mo-S in MoS_2 nanosheets. In addition to these appeared referred peaks in Fig. 2 b (ii), there are some other peaks that appeared at 1472, 1787, and 1197 cm^{-1} assigned to –C=C, –C=O, and –C–O functional groups of GQDs, respectively [36]. Moreover, the peaks found at 3202 and 1593 cm^{-1} are due to the O–H bonds and –C–C stretching in GQDs,

respectively. Furthermore, the immobilization of biomolecule on MoS_2@GQD surface was also confirmed by FT-IR spectra; data shown in Fig. 2 b (iii). The characteristic peaks found at 1723 and 3463 cm^{-1} correspond to the primary and secondary amide bonding, respectively [37], indicating the immobilization of antibody on MoS_2@GQDs/ITO composite.

Raman spectroscopy is the non-invasive and non-destructive technique which is widely used to identify the various chemical modification and structural defects. Raman spectrum is shown in Fig. 2 c, inset image; two characteristic modes such as in-plane (E_{2g}^1) mode and out-of-plane (A_{1g}) symmetric displacement appear in the wavelength region of 350 to 410 cm^{-1} corresponding to MoS_2 nanosheets [38]. The peak appeared at 381 cm^{-1} is due to the vibration of sulfur atoms in one direction and vibration of molybdenum atoms in another direction attributed to the existence of in-plane mode. In comparison, other dominant peaks appeared at 407 cm^{-1} correspond to another mode as out-of-plane symmetric displacement along the c-axis of sulfur atoms [38]. Moreover, the Raman spectrum of MoS_2@GQDs, as shown in Fig. 2 c, has well-defined characteristic peaks of MoS_2 nanosheets appearing at 389 and 403.8 cm^{-1} attributed to E_{2g}^1 and A_{1g} mode, respectively. However, peaks of modes of E_{2g}^1 and A_{1g} seem to be shifted towards higher and lower wavelength along with less frequency difference ($\Delta k \sim 14$) compared with peaks

that appeared in MoS_2 indicating the presence of few MoS_2 layers. Also, peaks found at 1368.5 and 1578.9 cm^{-1} correspond to D-band and G-band of GQDs, respectively, which can be assigned to K point phonons of A_{1g} symmetry and E_{2g} phonons of sp^2 bonds presenting between the carbon atoms [39]. The I_D/I_G ratio of peak intensity was found to be 0.46, indicating the presence of lower defects and lesser disorders in the structure of GQDs. However, a peak at 2891.1 cm^{-1} can be responsible for the 2D band in GQDs confirming the presence of relatively high-quality graphene with a large specific area. The ratio of I_G/I_{2D} band found to be 1.65 reveals that about 3 to 4 number of layers of GQDs are present. This formation of high-quality GQDs with a specific surface area is suitable for biosensing applications.

TEM micrographs of synthesized MoS_2 and MoS_2@GQD composites are shown in Fig. 3 a–h. Figure 3 a–c are the TEM images of exfoliated MoS_2 nanosheets, indicating the formation of single to multi-layered sheets of various sizes. HR-TEM lattice image has the interplanar distance of MoS_2 nanosheets shown in Fig. 3 c, which is found to be 0.69 nm, corresponding to the crystallographic spacing of (002) plane of MoS_2. Furthermore, TEM images of MoS_2@GQDs are depicted in Fig. 3 d–g clearly showing the presence of single to few layers of MoS_2 sheets along with small crystals of GQDs. The size of MoS_2 nanosheets lies in the range of 100 to 900 nm. The integration of nanocrystals of GQDs into MoS_2 nanosheets confirmed by HR-TEM analysis and

collected images is shown in Fig. 3 f and g. The presence of small grains of GQDs with an average diameter of 3 to 6 nm into the nanosheets of MoS_2 reveals the composite formation. Again, interplanar distance (0.69 nm) was found to be the same as observed in pristine MoS_2 nanosheets (Fig. 3c, f), and 0.23 nm of lattice spacing is observed, which corresponds to (002) orientation plane of GQDs. Also, selected area electron diffraction (SAED) of MoS_2@GQD composite was examined, and the pattern is shown in Fig. 3 h. The presence of (002), (100), (103), (105), and (110) indexed planes indicates the existence of polycrystalline nature that has different spots of arrangement inside the concentric circles [40].

After the structural confirmation of composite MoS_2@GQDs, the surface morphology of MoS_2@GQDs/ITO composite and immobilized biomolecules aAFB1/MoS_2@GQDs/ITO surface were examined by SEM technique. As shown in Fig. 4 a, the surface morphology of MoS_2@GQD composite shows dense, uniform, as well as the well-ordered distribution of particles over electrode surface along with the presence of some small spherical grains of nanocrystals on basal and edge planes of MoS_2, revealing the presence of GQDs. But after immobilization of antibody, aAFB1, over the MoS_2@GQDs film, surface morphology is transformed into the globular structure (Fig. 4b) from the dense and uniform surface. This transformation ascribed to the adsorption of antibodies of aAFB1 onto the composite surface and is the confirmation of the presence of antibodies.

Fig. 3 TEM images of synthesized (**a**–**c**) MoS_2, MoS_2@GQD composite (**d**–**g**) at different magnification and selected area of electron diffraction (SAED) pattern of MoS_2@GQDS (**h**)
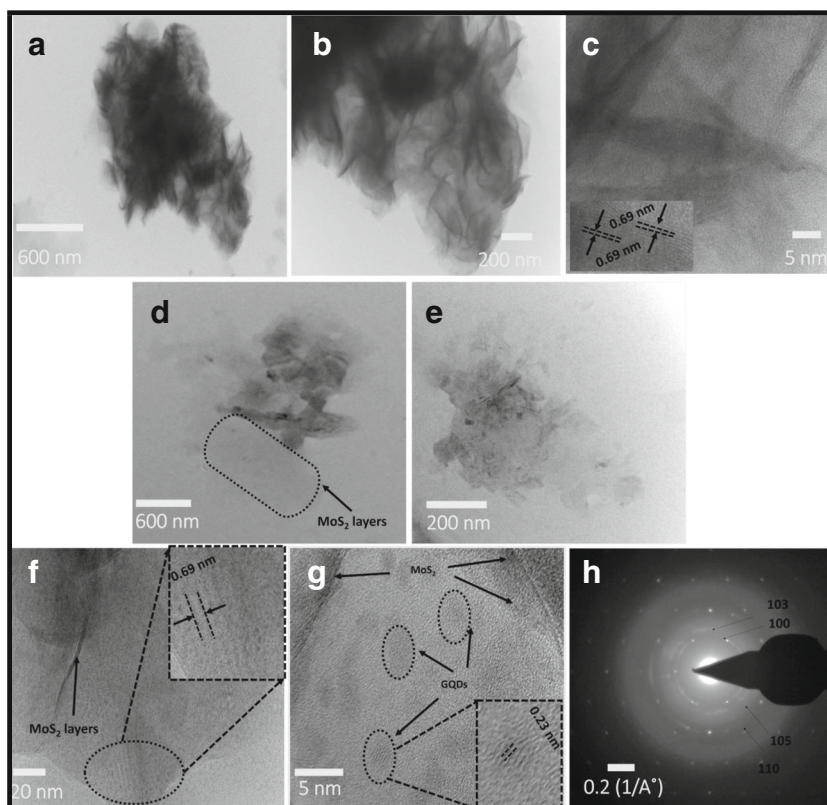
Fig. 4 SEM images of **a** MoS$_2$@GQDs/ITO electrode (inset image: zoom micrograph of MoS$_2$@GQD electrode) and **b** biomolecule aAFB1 immobilized on MoS$_2$@GQDs/ITO electrode
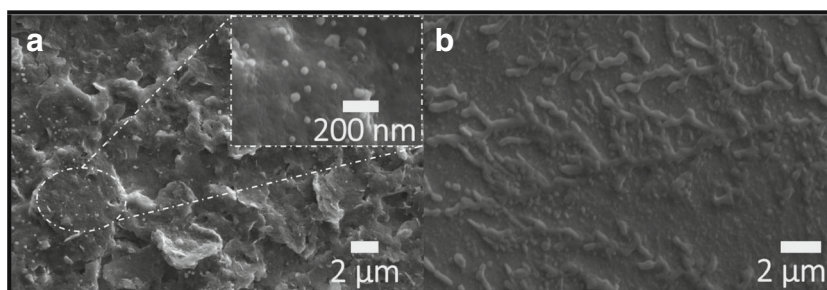
Zeta-potential studies were carried out to determine the overall charge on CTAB-MoS$_2$ nanosheets and MoS$_2$@GQD composite using Malvern Zetasizer (see ESM Fig. S2a, b). Zeta-potential of CTAB-MoS$_2$ nanosheets is found to be + 25.8 mV indicating the presence of positive charge due to CTAB over MoS$_2$ nanosheets (see ESM Fig. S2a), while Zeta-potential of GQDs and MoS$_2$@GQD nanosheets is found to be − 10.0 mV (previously reported an article by Bhardwaj et al. 2018) and 0.42 mV (see ESM Fig. S2b), respectively. These results indicate that GQDs can be attached directly with CTAB-MoS$_2$ nanosheets due to differences in the surface potential results in electrostatic interaction between them.

Electrochemical analytical studies

Electrochemical behavior at the electrode/electrolyte interface was examined by the EIS technique. EIS is a label-free, simple, and powerful tool to study the transport process, interaction, and adsorption behavior of biomolecules with the electrode surface [41]. EIS analyzer is a potentiostat designed mainly to measure AC impedance as a function of frequency ranging from 0.1 to 10^4 Hz, and their spectrum obtained in the form of Nyquist plot containing semicircle diameter and linear portion. The diameter of the semicircle represents the behavior of resistance in charge transfer, which is observed towards a higher frequency region. In contrast, the mass transfer process appeared at a lower frequency region by applying a small perturbation voltage to the electrochemical cell that contains electrodes and electroactive species [41]. Generally, the Randles equivalent circuit is used for the analysis of the Nyquist plot. This circuit comprised an active electrolyte or solution resistance (R$_S$) in series with a parallel combination of the double-layer capacitor (C$_{dl}$), Warburg impedance of a faradaic reaction. Using the equivalent circuit fitting function, several relevant electrochemical parameters can be identified to examine the sensor performance. Before conducting electrical analytical studies, all the electrical connections are mechanically tighten to ensure that no resistance dissipation in the form of heat occurs. Because loose connections of the ITO conductive surface result corrosion and develop resistance across the connections. This resistance generally dissipates the power in the form of heat when the current flows through

a wire, and it directly impacts on the quality of the electrochemical signal [42].

Electrochemical measurements of the different electrodes were investigated by the EIS analyzer. Figure 5 a illustrates electrochemical impedance behavior of bare ITO (curve i) and modified electrodes such as MoS$_2$/ITO (curve ii, 206.52 Ω), MoS$_2$@GQDs/ITO (curve iii, 117.5 Ω), aAFB1/MoS$_2$/ITO (curve iv, 239.93 Ω), and aAFB1/MoS$_2$@GQDs/ITO (curve v, 515.24 Ω) measurements were conducted in PBS (50 mM 0.9% NaCl) containing 5 mM redox probe [Fe(CN)$_6$]$^{3−/4−}$ pH 7.4 using EIS technique. The R$_{CT}$ value of MoS$_2$@GQDs/ITO electrode found to be lower compared with the MoS$_2$/ITO electrode could be attributed to GQDs which act as a mediator for electron transfer with more exposed sites and improved surface area that shortens the diffusion pathway of electrons which promotes the charge transfer and interdomain conductivity [43, 44]. After immobilization of antibody, aAFB1, on MoS$_2$@GQDs/ITO electrode, the R$_{CT}$ value is increased to 515.24 Ω in comparison with 239.93 Ω of AFB1/MoS$_2$/ITO electrode. This significant increment in the value of R$_{CT}$ of aAFB1/MoS$_2$@GQDs/ITO electrode may be ascribed to the integration of GQDs into MoS$_2$ nanosheets. The surface coverage of these electrodes has been calculated using the relation $\theta = 1-R_{CT}$ (electrode)/R$_{CT}$ (bioelectrode), where θ is the fraction of occupied binding sites and charge transfer resistance (R$_{CT}$) of electrode and bioelectrode, before and after immobilization of antibody, respectively. The θ of MoS$_2$-based immunoelectrode with and without GQDs was 78% and 20%, respectively. Incorporation of GQDs into MoS$_2$ may be responsible for the maximum coverage of antibodies on the MoS$_2$@GQDs electrode surface. Interestingly, the MoS$_2$@GQDs surface provides more conducive functional groups and a large surface-to-volume ratio to bind a large number of antibodies. Non-conducting bulky groups present in the antibodies conjugating over the MoS$_2$@GQDs electrode hinder the electron transfer between electrode and electrolyte redox probe, thus effectively reducing electron transfer rate and correspondingly increasing R$_{CT}$ value.

The K-K test was used to evaluate the impedance data quality of Fig. 5 a using the K-K function in the Autolab instrument. One frequency per decade extension and complex type of test was applied. In general, pseudo-chi-square (χ^2)

Fig. 5 **a** EIS studies of (i) ITO, (ii) MoS_2/ITO, (iii) MoS_2@GQDs/ITO, (iv) aAFB1/MoS_2/ITO, and (v) aAFB1/MoS_2@GQDs/ITO electrodes conducted in PBS (50 mM, pH 7.4) containing $[Fe(CN)_6]^{3-/4-}$ (inset image: Randles equivalent circuit). **b** CV studies as a function of scan rate from 10 to 100 mV s^{-1} conducted in 50 mM PBS (pH 7.4) containing 5 mM $[Fe(CN)_6]^{3-/4-}$ (inset image: (ii) and (iii) represent the anodic peak current and cathodic peak current vs. square root of the scan rate of aAFB1/MoS_2/ITO electrode whereas curves (i) and (iv) are aAFB1/MoS_2@GQDs/ITO electrode). **c** EIS response of aAFB1/MoS_2@GQDs/ITO electrode as a function of antigen concentration from 0.1–3.0 ng/mL (0.1, 0.5, 1.0, 1.5, 2.0, 2.5, and 3.0 ng/mL). **d** Calibration plot of ΔR_{CT} value as a function of AFB1 concentration from 0.1 to 3.0 ng/mL
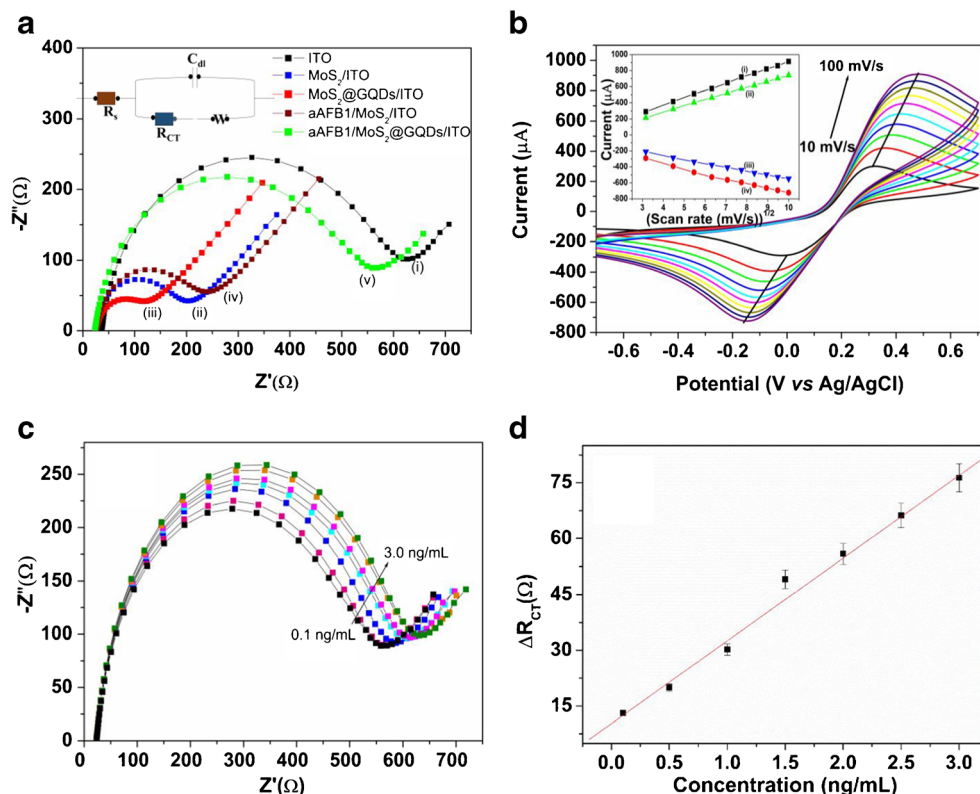
values are used to check the quality of impedance data. It is found that the χ^2 value of all the fabricated electrodes (MoS_2/ITO, aAFB1/MoS_2/ITO, MoS_2@GQDs/ITO, and aAFB1/MoS_2@GQDs/ITO) lies in the range of 10^{-5} to 10^{-6} revealing that impedance data quality is reasonable. Moreover, computer-simulated fitting was performed on the impedance spectra of aAFB1/MoS_2@GQDs/ITO electrode using different electronic circuit elements to attain the best fit of spectra based on the Randles equivalent circuit (Fig. 5a: inset image). It is observed that circuit elements are $R_s(C_{dl}[R_{CT}Zw])$ attained with a low percentage of error.

Also, electrochemical properties such as dielectric properties and interaction with biomolecules were investigated by the EIS technique on MoS_2/ITO, aAFB1/MoS_2/ITO, MoS_2@GQDs/ITO, and aAFB1/MoS_2@GQDs/ITO electrodes. The C_{dl} value of immobilized antibody electrodes such as aAFB1/MoS_2/ITO (29 μF) and aAFB1/MoS_2@GQDs/ITO (44 μF) is found to be lower compared with MoS_2/ITO (88 μF) and MoS_2@GQDs/ITO (76 μF) electrodes. After the immobilization of antibodies, a decrease in the C_{dl} value is observed due to the formation of an interface between the electrode and electrolyte redox probe. And the distance between electrode and electrolyte interface increases resulting a decrement in the total capacitance value.

Another important parameter is the HET rate constant value which was also calculated to determine the electrochemical characteristics of different fabricated electrodes. This constant value tells us about the rate of transfer of an electron between

the electrode surface matrix and the redox probe as a chemical species. This important parameter not only allows us to know about the interfacial interaction of the structural features of the sensing interface but also explains the mechanisms of a chemical process occurring at the electrode/electrolyte interface. HET values of fabricated electrodes of MoS_2/ITO, MoS_2@GQDs/ITO, aAFB1/MoS_2/ITO, and aAFB1/MoS_2@GQDs/ITO were calculated using Eq. [1] [45]

$$K_e = \frac{RT}{n^2 F^2 A R_{CT} S} \qquad (1)$$

Here, R represents gas constant (8.314 JK^{-1} mol^{-1}), T for temperature (298 K), n is a number of electron transfer ($n = 1$), F represents Faraday constant (96,500 C mol^{-1}), A is an effective area of the electrode (0.5 cm^2), the R_{CT} (Ω), and C is for the concentration of redox species (5 mM). HET value for MoS_2/ITO electrode was found to be 5.0×10^{-5} cm/s whereas HET value for MoS_2@GQDs/ITO electrode was found to be 9.0×10^{-5} cm/s. HET rate constant value seems to be approximately two times higher with composite MoS_2@GQDs than MoS_2 alone, which is due to the presence of significant energy band gap in MoS_2@GQDs, low R_{CT} value, that provides the easiest path for electronic transportation between electrode and electrolyte system. Therefore, GQD nanocrystals on MoS_2 nanosheets are beneficial for mass transfer electroactive species, stabilization, and effective conjugation with biomolecules [46]. However, HET value is found to significantly decrease

after the immobilization of antibody aAFB1 on MoS$_2$@GQDs/ITO (2.064×10^{-5} cm/s) compared with MoS$_2$/ITO electrode (4.435×10^{-5} cm/s) because of bulky groups present in the structure of antibody that provide hindrance in transferring the electron between modified electrode and electrolyte. The presence of a large number of antibody on the electrode surface also interrupts the electron transfer rate constant.

Following this EIS characterization, CV studies were also carried out to further characterize the surface of the electrodes such as MoS$_2$/ITO, MoS$_2$@GQDs/ITO, and aAFB1/MoS$_2$@GQDs/ITO electrodes in PBS (50 mM, pH 7.4) containing 5 mM of [Fe(CN)$_6$]$^{3-/4-}$ at scan rate (50 mV/s) under the potential range of -0.75 V to $+0.75$ V (see ESM Fig. S3). The anodic peak current of MoS$_2$/ITO is found to be 640 μA because of the MoS$_2$ nanosheets, while in the case of MoS$_2$@GQDs/ITO electrode, well-defined oxidation and reduction peaks are obtained at 1177 μA and -990 μA. Noticeably, the current response of MoS$_2$@GQDs/ITO electrode is higher compared with the MoS$_2$/ITO electrode, ascribed to the larger surface area, excellent adhesion, good permeability as well as high electrocatalytic activity of GQDs that facilitate the electron transfer efficiency and electrochemical activity between the solution and the electrode surface. However, after the immobilization of antibody aAFB1 on MoS$_2$@GQDs/ITO electrode, anodic peak current is decreased to 613 μA, due to the loading of the antibody that creates hindrance in transferring the electron.

Figure 5 b illustrates CV scan rate studies of modified electrodes aAFB1/MoS$_2$@GQDs/ITO and aAFB1/MoS$_2$/ITO as a function of scan rate from 10 to 100 mV/s (triplicate experiment was performed under the same experimental conditions). The magnitude of the anodic, as well as cathodic peak current and potential response, holds a linear relation with a gradual change in scan rate, suggesting a diffusion-controlled process with facile charge transfer kinetics. And the value of E$_p$ increases as increasing the scan rate disclosing electron transfer kinetics has a quasi-reversible process, and faster scan rate leads to a decrease in the size of the diffusion layer. Inset image of Fig. 5 b shows the linear response of the anodic and cathodic peak current varied linearly with the square root of the scan rate. The linear regression equation [2–5] are given,

$$I_a = 10.02355 \mu A + 90.4062 \mu A/[mV/s]^{1/2}$$
$$\times \text{ scan rate } [mV/s]^{-1/2}, R^2$$
$$= 0.9994 \tag{2}$$

$$I_c = -118.644 \ \mu A - 61.366 \ \mu A/[mV/s]^{1/2}$$
$$\times \text{ scan rate } [mV/s]^{-1/2}, R^2$$
$$= 0.9916 \tag{3}$$

$$I_a = -18.0855 \ \mu A + 76.13569 \ \mu A/[mV/s]^{1/2}$$
$$\times \text{ scan rate } [mV/s]^{-1/2}, R^2$$
$$= 0.9994 \tag{4}$$

$$I_c = -63.27854 \mu A - 48.85628 \ \mu A/[mV/s]^{1/2} \tag{5}$$
$$x \text{ scan rate } [mV/s]^{-1/2}, R^2 = 0.9982$$

Here, R^2 is the regression coefficient, and SD is the standard deviation.

Current passing through the electrode is limited by the diffusion species to the electrode, and diffusion flux is influenced by the concentration gradient near the electrode. Thus, concentration gradient is affected by the concentration species at the electrode, and linear variation indicated the diffusion ability through a solution. By changing the cell voltage, the concentration of species at electrode surface changes; therefore, the voltage sweeps cause a more significant concentration gradient resulting in higher current observed.

The diffusion coefficient of aAFB1/MoS$_2$@GQDs/ITO electrode was found to be 1.67×10^{-5} cm^2/s which was calculated by Randles-Sevcik (Eq. [6]) [47],

$$I_p = 2.69x10^5 n^{3/2} A D^{1/2} V^{1/2} C \tag{6}$$

where I_p stands for a peak current of bioelectrode (A), n for number of electrons involved in the reaction ($n = 1$), C stands for the concentration of redox species (5 mM), A is the active surface area of the electrode (0.5 cm^2), D represents the diffusion coefficient, and V for scan rate (50 mV s^{-1}). Moreover, all the relevant electrochemical parameter values like C$_{dl}$, R$_{CT}$, and HET of surface-modified electrodes are summarized in ESM Table S1; here, MoS$_2$@GQD composite shows low R$_{CT}$ and fast HET rate constant.

Optimization of aAFB1 concentration

The optimization of the required antibody on the fabricated surface matrix plays a significant role in influencing the sensitivity of the immunosensor. Therefore, the subsequent amount of antibody was studied with a series concentration ranging from 20 to 120 μg/mL using electrochemical impedance spectroscopy, and obtained results are depicted in ESM Fig. S4. It is found that with increasing aAFB1 concentration from 20 to 120 μg/mL, the impedance response signal increases up to a concentration of 80 μg/mL antibody. By further increasing the concentration of aAFB1, the R$_{CT}$ value slightly tends to decrease. This may be attributed to molecular bonding occurring between the antibody and electrode surface material, which get saturated after 80 μg/mL. This saturation trend indicates that further, no more binding sites available on the electrode surface resulted in creating hindrance; therefore, impedance signal decreases [48]. So, antibody aAFB1

concentration for MoS_2@GQDs/ITO electrode was optimized at 80 μg/mL and used for further experimental studies.

Analytical performance of immunosensor

Electrochemical biosensing performance for AFB1 detection was carried out with various AFB1 antigen concentration ranging from 0.1 to 3.0 ng/mL using EIS technique in 50 mM PBS (pH 7.4) containing 5 mM $[Fe(CN)_6]^{3-/4-}$ (Fig. 5c,d). Figure 5 c represents the electrochemical impedance sensing response as a function of AFB1 antigen concentrations (0.1 to 3.0 ng/mL). It is clearly showing that the semicircle diameter of the Nyquist plot increases by increasing the AFB1 concentration indicating AFB1 biomolecules are readily interact with aAFB1/MoS_2@GQD surface due to antigen-antibody immunocomplex formation. This immunocomplex reveals that the electrode surface gets overcrowded, thus creating an inert electron as well as mass transfer interfacial layer that affects the transportation of $[Fe(CN)_6]^{3-/4}$. Thus, R_{CT} value increases with increasing the AFB1 concentration. On further increment in AFB1 concentration, change in impedance response gets saturated by attaining a steady-state behavior, indicating no more availability of antigen-binding sites on fabricated aAFB1/MoS_2@GQD immunoelectrode.

Furthermore, a calibration plot between change in ΔR_{CT} response as a function of AFB1 concentration is depicted in Fig. 5 d. The linear equation obtained from the calibration plot by a linear fit function is $\Delta R_{CT} = 10.30 + 22.22 \times$ concentration (ng/mL) with a linear regression coefficient value (R) of 0.99; the standard deviation is 1.45 and statistically highly significant as p value < 0.0001. The limit of detection of this fabricated immunosensor was 0.09 ng/mL, calculated using a standard formula $3^{\sigma}/_m$; here, σ is the standard deviation and m is the slope. The sensitivity of the immunosensor was found to be 44.44 $\Omega/(ng\ mL^{-1})/cm^2$. Better and remarkable increases in electrochemical properties and biosensing characteristics have been found mainly due to the influence of MoS_2@GQD composite transducer material for the fabrication of immunosensor. An ionic surfactant such as CTAB shows decisive role in conjugating the two negative species such as GQDs and negatively charged MoS_4^{2-} material by minimizing the electrostatic repulsion between them [46]. Intriguingly, graphene-based nanocrystals having abundant oxygenated functional groups lead to interact interestingly with positive species of cationic surfactant MoS_2 nanosheets, and thus, it formed a well-dispersed aqueous composite [49].

Earlier, we have published research work for AFB1 detection using the GQD-AuNP surface matrix by cyclic voltammetry technique. Though the sensor has shown high performance for the detection of food toxin, in the case of low concentration, the significant linear change in the

voltammetry peak height has been obtained [5]. As by increasing the AFB1 concentration, voltammetry waves are merged and migrated towards the higher potential side due to the electron transfer kinetics of the quasi-reversible process. Shelf-life of the immunosensor showed 6% decrement in the 2nd week and 34% decrement in the 5th week from the initial response signal. However, in the current article, a 2D layered structure has been used as a surface matrix for the fabrication of AFB1 biosensor. MoS_2@GQD-based immunosensor showed 78% coverage of antibodies revealed the strong bio-nano conjugation due to the presence of a two-dimensional layered structure that provides a large surface area for immobilization of antibody. HET rate constant was found 5.0×10^{-5} cm/s for MoS_2/ITO electrode, for MoS_2@GQDs/ITO was 9.0×10^{-5} cm/s, and after the immobilization of aAFB1 on MoS_2@GQDs/ITO was 2.064×10^{-5} cm/s. HET rate constant value seems to be approximately two times higher. It happens due to the low R_{CT} value in MoS_2@GQDs which provides the easiest path for electronic transportation between electrode and electrolyte systems. The MoS_2@GQDs/ITO-based biosensor was able to detect AFB1 in the linear range of 0.1 to 3.0 ng/mL with a limit of detection of 0.09 ng/mL. Also, the electrochemical performance of the fabricated immunosensor is compared with the earlier reported AFB1 sensor, which is summarized in a tabular form ESM Table S2 [5, 50–56]. From this table, it can be concluded that electrochemical parameters are comparable with other fabricated immunosensor.

Real sample analysis

The reliability of the fabricated immunosensor for real-time analysis is also one of the advantageous characteristics that imply the analytical performance of the sensor. To carry out real sample analysis using fabricated aAFB1/MoS_2@GQDs/ITO electrode, non-spiked and spiked maize samples were used, and electrochemical measurements were carried out using the EIS technique. Results obtained from this study are summarized in ESM Table S3, which shows that percentage recovery lies in the range of 80.2–98.3%, indicating the precise performance of the sensor for AFB1 detection in maize. Moreover, the low values of relative standard deviation (RSD) of less than 6% indicated an excellent precision and acceptability of the fabricated biosensor for testing of AFB1 in maize. Thus, it can be concluded that nanocomposite-based biosensor for AFB1 detection attained a better recovery rate, which is highly suitable for maize sample analysis.

Reproducibility, interference, and shelf-life studies

Reproducibility studies of fabricated aAFB1/MoS_2@GQDs/ITO immunosensor were also carried out using the four similarly prepared electrodes with respect to AFB1 concentration of 0.5 ng/mL. A negligible change in the impedance response

is observed with all four fabricated electrodes (see ESM Fig. S5a) with low RSD (1.18%), and coefficient of variation value (1.02%) indicates good precision and reproducibility of MoS_2@GQD-based biosensor for AFB1 detection.

To evaluate the specificity of fabricated aAFB1/ MoS_2@GQDs/ITO immunoelectrode, potential interferent studies were carried out using AFB1 and ochratoxin A antigen analytes. Different concentrations of ochratoxin A (0.1 and 0.5 ng/mL) and AFB1 (0.1 ng/mL) were used, and measurements were carried out using the EIS technique. The results are depicted in ESM Fig. S5b. About 1.2% change in R_{CT} value is observed with AFB1 and ochratoxin A (1:1 (v/v) of 0.1 ng/mL), whereas with a higher concentration of ochratoxin A (0.5 ng/mL), about 1.98% change in the R_{CT} value is found. Thus, this change may be due to the non-specific binding of ochratoxin A with aAFB1/MoS_2@GQDs/ITO electrode resulting in insignificant variation in the impedance response signal. So, this study concludes that aAFB1/ MoS_2@GQDs/ITO electrode did not show any cross-reactivity with ochratoxin A and provides high specificity to the fabricated sensor.

Shelf-life studies of the fabricated aAFB1/MoS_2@GQDs/ ITO electrode was investigated by measuring the electrochemical impedance response signal in the interval of every 5 days for consecutive 30 days. After conducting the experiments, the electrode was stored in a refrigerator at 4 °C. ESM Fig. S5c represents the stability response of the bioelectrode. An insignificant change in R_{CT} value is observed in initial days, even up to 15 days or 2nd week (4% decrease in signal). Still, after 20 days, about 10% decrement in the response signal is observed, and on continuous measuring until 30 days, about 26% decrement in the response signal attributed towards the conducive morphology as well as an effective conjugation of biomolecules with MoS_2@GQDs electrode surface that improves stability factor of the biosensor.

Conclusions

In this study, we prepared GQD-decorated CTAB-MoS_2 nanosheet using a chemical process to improve the electro-optical properties of the material. Structural and morphological studies confirmed the formation of a nanomaterial as well as the successive surface modifications of the electrode. EIS and CV techniques were used for electrochemical characterization. The fabricated electrode of aAFB1/MoS_2@GQDs/ ITO was successfully utilized for AFB1 detection ranging from 0.1 to 3.0 ng/mL with a limit of detection of 0.09 ng/ mL. Selective and sensible immunosensor for AFB1 detection demonstrate the role of MoS_2@GQD electrode as a transducer material. Facile combination of MoS_2@GQDs is well-suited for the fabrication of biosensor because it improved the surface-to-volume ratio, excellent electronic conductivity,

good biocompatibility, abundant functional groups of moieties for direct electron transfer process and led to achieve good electrocatalytic properties. Real maize sample analysis was performed with spiked samples of different AFB1 concentrations, and percentage recoveries were found to be acceptable. Efforts should be made to utilize this immunosensor for designing and detection of other mycotoxins.

Compliance with ethical standards

Conflict of interest The authors declare that they have no conflicts of interest.

Ethical approval This article does not contain any studies related to human participants or animal performed by any authors.

References

1. Moretti A, Logrieco AF, Susca A. Mycotoxins: an underhand food problem. Mycotoxigenic Fungi: Springer; 2017. p. 3–12.
2. Abbas HK, Accinelli C, Shier WT. Biological control of aflatoxin contamination in U.S. crops and the use of bioplastic formulations of Aspergillus flavus biocontrol strains to optimize application strategies. J Agric Food Chem. 2017;65(33):7081–7.
3. Neme K, Mohammed A. Mycotoxin occurrence in grains and the role of postharvest management as a mitigation strategies. A review. Food Control. 2017;78:412–25.
4. Guo W, Wu L, Fan K, Nie D, He W, Yang J, et al. Reduced graphene oxide-gold nanoparticle nanoframework as a highly selective separation material for aflatoxins. Sci Rep. 2017;7(1): 14484.
5. Bhardwaj H, Pandey MK, Rajesh, Sumana G. Electrochemical aflatoxin B1 immunosensor based on the use of graphene quantum dots and gold nanoparticles. Microchim Acta. 2019;186(8):592.
6. Guan Z, Lian C-S, Hu S, Ni S, Li J, Duan W. Tunable structural, electronic, and optical properties of layered two-dimensional C2N and MoS2 van der Waals heterostructure as photovoltaic material. J Phys Chem C. 2017;121(6):3654–60.
7. Hoshide T, Zheng Y, Hou J, Wang Z, Li Q, Zhao Z, et al. Flexible lithium-ion fiber battery by the regular stacking of two-dimensional titanium oxide nanosheets hybridized with reduced graphene oxide. Nano Lett. 2017;17(6):3543–9.
8. Seh ZW, Fredrickson KD, Anasori B, Kibsgaard J, Strickler AL, Lukatskaya MR, et al. Two-dimensional molybdenum carbide (MXene) as an efficient electrocatalyst for hydrogen evolution. ACS Energy Lett. 2016;1(3):589–94.
9. Huang K-J, Liu Y-J, Wang H-B, Wang Y-Y, Liu Y-M. Sub-femtomolar DNA detection based on layered molybdenum disulfide/multi-walled carbon nanotube composites, Au nanoparticle and enzyme multiple signal amplification. Biosens Bioelectron. 2014;55:195–202.
10. Koppens FHL, Mueller T, Avouris P, Ferrari AC, Vitiello MS, Polini M. Photodetectors based on graphene, other two-dimensional materials and hybrid systems. Nat Nanotechnol. 2014;9:780.

11. Song Y, Luo Y, Zhu C, Li H, Du D, Lin Y. Recent advances in electrochemical biosensors based on graphene two-dimensional nanomaterials. Biosens Bioelectron. 2016;76:195–212.

12. Chen Y, Fan Z, Zhang Z, Niu W, Li C, Yang N, et al. Two-dimensional metal nanomaterials: synthesis, properties, and applications. Chem Rev. 2018;118(13):6409–55.

13. Su S, Sun H, Cao W, Chao J, Peng H, Zuo X, et al. Dual-target electrochemical biosensing based on DNA structural switching on gold nanoparticle-decorated MoS2 nanosheets. ACS Appl Mater Interfaces. 2016;8(11):6826–33.

14. Huang J, He Y, Jin J, Li Y, Dong Z, Li R. A novel glucose sensor based on MoS2 nanosheet functionalized with Ni nanoparticles. Electrochim Acta. 2014;136:41–6.

15. Ataca C, Ciraci S. Functionalization of single-layer MoS honeycomb structures. J Phys Chem C. 2011;115(27):13303–11.

16. Vilian AE, Dinesh B, Kang S-M, Krishnan UM, Huh YS, Han Y-K. Recent advances in molybdenum disulfide-based electrode materials for electroanalytical applications. Microchim Acta. 2019;186(3):203.

17. Gupta A, Arunachalam V, Vasudevan S. Water dispersible, positively and negatively charged MoS2 nanosheets: surface chemistry and the role of surfactant binding. J Phys Chem Lett. 2015;6(4):739–44.

18. McAteer D, Gholamvand Z, McEvoy N, Harvey A, O'Malley E, Duesberg GS, et al. Thickness dependence and percolation scaling of hydrogen production rate in MoS2 nanosheet and nanosheet–carbon nanotube composite catalytic electrodes. ACS Nano. 2016;10(1):672–83.

19. Li Z, Ye R, Feng R, Kang Y, Zhu X, Tour JM, et al. Graphene quantum dots doping of MoS2 monolayers. Adv Mater. 2015;27(35):5235–40.

20. Zhang Z, Zhang J, Chen N, Qu L. Graphene quantum dots: an emerging material for energy-related applications and beyond. Energy Environ Sci. 2012;5(10):8869–90.

21. Yan X, Song Y, Zhu C, Song J, Du D, Su X, et al. Graphene quantum dot–MnO2 nanosheet based optical sensing platform: a sensitive fluorescence "Turn Off–On" nanosensor for glutathione detection and intracellular imaging. ACS Appl Mater Interfaces. 2016;8(34):21990–6.

22. Lukowski MA, Daniel AS, Meng F, Forticaux A, Li L, Jin S. Enhanced hydrogen evolution catalysis from chemically exfoliated metallic MoS2 nanosheets. J Am Chem Soc. 2013;135(28):10274–7.

23. Zhang S-L, Yue H, Liang X, Yang W-C. Liquid-phase Co-exfoliated graphene/MoS2 nanocomposite for methanol gas sensing. J Nanosci Nanotechnol. 2015;15(10):8004–9.

24. Coleman JN, Lotya M, O'Neill A, Bergin SD, King PJ, Khan U, et al. Two-dimensional nanosheets produced by liquid exfoliation of layered materials. Science. 2011;331(6017):568.

25. Bhardwaj H, Singh C, Kotnala R, Sumana G. Graphene quantum dots-based nano-biointerface platform for food toxin detection. Anal Bioanal Chem. 2018;410(28):7313–23.

26. Bhardwaj H, Singh C, Pandey M, Sumana G. Star shaped zinc sulphide quantum dots self-assembled monolayers: preparation and applications in food toxin detection. Sensors Actuators B Chem. 2016;231:624–33.

27. Bhardwaj H, Sumana G, Marquette CA. A label-free ultrasensitive microfluidic surface plasmon resonance biosensor for aflatoxin B1 detection using nanoparticles integrated gold chip. Food Chem. 2020;307:125530.

28. Park JH, Kim Y-P, Kim I-H, Ko S. Rapid detection of aflatoxin B1 by a bifunctional protein crosslinker-based surface plasmon resonance biosensor. Food Control. 2014;36(1):183–90.

29. Tralamazza SM, Bemvenuti RH, Zorzete P, de Souza GF, Corrêa B. Fungal diversity and natural occurrence of deoxynivalenol and zearalenone in freshly harvested wheat grains from Brazil. Food Chem. 2016;196:445–50.

30. Cole RJ, Cox RH. Handbook of toxic fungal metabolites. Academic Press; 1981.

31. Zhao XS, Kong WJ, Wang S, Wei JH, Yang MH. Simultaneous analysis of multiple mycotoxins in Alpinia oxyphylla by UPLC-MS/MS. World Mycotoxin J. 2017;10(1):41–51.

32. Wang D, Song L, Zhou K, Yu X, Hu Y, Wang J. Anomalous nano-barrier effects of ultrathin molybdenum disulfide nanosheets for improving the flame retardance of polymer nanocomposites. J Mater Chem A. 2015;3(27):14307–17.

33. Mukherjee S, Maiti R, Midya A, Das S, Ray SK. Tunable direct bandgap optical transitions in MoS2 nanocrystals for photonic devices. ACS Photonics. 2015;2(6):760–8.

34. Li Y, Wang J, Tian X, Ma L, Dai C, Yang C, et al. Carbon doped molybdenum disulfide nanosheets stabilized on graphene for the hydrogen evolution reaction with high electrocatalytic ability. Nanoscale. 2016;8(3):1676–83.

35. Zhou K, Liu J, Zeng W, Hu Y, Gui Z. In situ synthesis, morphology, and fundamental properties of polymer/MoS2 nanocomposites. Compos Sci Technol. 2015;107:120–8.

36. Wang C, Jin J, Sun Y, Yao J, Zhao G, Liu Y. In-situ synthesis and ultrasound enhanced adsorption properties of MoS2/graphene quantum dot nanocomposite. Chem Eng J. 2017;327:774–82.

37. Ali MA, Kamil Reza K, Srivastava S, Agrawal VV, John R, Malhotra BD. Lipid–lipid interactions in aminated reduced graphene oxide interface for biosensing application. Langmuir. 2014;30(14):4192–201.

38. Yan Y, Ge X, Liu Z, Wang J-Y, Lee J-M, Wang X. Facile synthesis of low crystalline MoS 2 nanosheet-coated CNTs for enhanced hydrogen evolution reaction. Nanoscale. 2013;5(17):7768–71.

39. Liu Y-M, Zhou M, Liu Y-Y, Huang K-J, Cao J-T, Zhang J-J, et al. A novel sandwich electrochemiluminescence aptasensor based on molybdenum disulfide nanosheet–graphene composites and Au nanoparticles for signal amplification. Anal Methods. 2014;6(12):4152–7.

40. Hu SW, Yang LW, Tian Y, Wei XL, Ding JW, Zhong JX, et al. Non-covalent doping of graphitic carbon nitride with ultrathin graphene oxide and molybdenum disulfide nanosheets: an effective binary heterojunction photocatalyst under visible light irradiation. J Colloid Interface Sci. 2014;431:42–9.

41. Ohno R, Ohnuki H, Wang H, Yokoyama T, Endo H, Tsuya D, et al. Electrochemical impedance spectroscopy biosensor with interdigitated electrode for detection of human immunoglobulin A. Biosens Bioelectron. 2013;40(1):422–6.

42. Veth C, Dragicevic D, Merten C. Thermal characterizations of a large-format lithium ion cell focused on high current discharges. J Power Sources. 2014;267:760–9.

43. Guo T, Wang L, Sun S, Wang Y, Chen X, Zhang K, et al. Layered MoS2@ graphene functionalized with nitrogen-doped graphene quantum dots as an enhanced electrochemical hydrogen evolution catalyst. Chin Chem Lett. 2019;30(6):1253–60.

44. Guo B, Yu K, Li H, Qi R, Zhang Y, Song H, et al. Coral-shaped MoS2 decorated with graphene quantum dots performing as a highly active electrocatalyst for hydrogen evolution reaction. ACS Appl Mater Interfaces. 2017;9(4):3653–60.

45. Song D, Wang Y, Lu X, Gao Y, Li Y, Gao F. Ag nanoparticles-decorated nitrogen-fluorine co-doped monolayer MoS2 nanosheet for highly sensitive electrochemical sensing of organophosphorus pesticides. Sensors Actuators B Chem. 2018;267:5–13.

46. Vasilescu I, Eremia SAV, Kusko M, Radoi A, Vasile E, Radu G-L. Molybdenum disulphide and graphene quantum dots as electrode modifiers for laccase biosensor. Biosens Bioelectron. 2016;75:232–7.

47. Balasubramanian P, Balamurugan TST, Chen S-M, Chen T-W, Lin P-H. A novel, efficient electrochemical sensor for the detection of

isoniazid based on the B/N doped mesoporous carbon modified electrode. Sensors Actuators B Chem. 2019;283:613–20.

48. Chandra S, Gäbler C, Schliebe C, Lang H, Bahadur D. Fabrication of a label-free electrochemical immunosensor using a redox active ferrocenyl dendrimer. New J Chem. 2016;40(11):9046–53.

49. Wang Z, Chen T, Chen W, Chang K, Ma L, Huang G, et al. CTAB-assisted synthesis of single-layer MoS 2–graphene composites as anode materials of Li-ion batteries. J Mater Chem A. 2013;1(6): 2202–10.

50. Srivastava S, Ali MA, Umrao S, Parashar UK, Srivastava A, Sumana G, et al. Graphene oxide-based biosensor for food toxin detection. Appl Biochem Biotechnol. 2014;174(3):960–70.

51. Srivastava S, Kumar V, Ali MA, Solanki PR, Srivastava A, Sumana G, et al. Electrophoretically deposited reduced graphene oxide platform for food toxin detection. Nanoscale. 2013;5(7):3043–51.

52. Kalita P, Singh J, Kumar Singh M, Solanki PR, Sumana G, Malhotra B. Ring like self assembled Ni nanoparticles based biosensor for food toxin detection. Appl Phys Lett. 2012;100(9): 093702.

53. Yagati A, Chavan S, Baek C, Lee M-H, Min J. Label-free impedance sensing of aflatoxin B1 with polyaniline nanofibers/Au nanoparticle electrode array. Sensors. 2018;18(5):1320.

54. Foguel M, Furlan Giordano G, de Sylos C, Carlos I, Pupim Ferreira A, Benedetti A, et al. A low-cost label-free AFB1 impedimetric immunosensor based on functionalized CD-trodes. Chemosensors. 2016;4(3):17.

55. Li Z, Ye Z, Fu Y, Xiong Y, Li Y. A portable electrochemical immunosensor for rapid detection of trace aflatoxin B 1 in rice. Anal Methods. 2016;8(3):548–53.

56. Masoomi L, Sadeghi O, Banitaba MH, Shahrjerdi A, Davarani SSH. A non-enzymatic nanomagnetic electro-immunosensor for determination of aflatoxin B1 as a model antigen. Sensors Actuators B Chem. 2013;177:1122–7.